1/3 plateau and 3/5 discontinuity in the magnetization and the magnetic phase diagram of hexagonal $GdInO_3$

N. Yuan,* A. Elghandour, W. Hergett, R. Ohlendorf, L. Gries, and R. Klingeler†
Kirchhoff Institute of Physics, Heidelberg University, INF 227, D-69120 Heidelberg, Germany

(Received 9 August 2023; revised 14 November 2023; accepted 15 November 2023; published 1 December 2023)

We report the high-pressure optical floating-zone growth of $GdInO_3$ single crystals and show its magnetic phase diagram down to the millikelvin regime as determined by magnetization measurements. The centered-honeycomb lattice structure shows considerable magnetic frustration ($|\Theta|/T_N \simeq 5$) and develops long-range magnetic order below $T_N = 2.1$ K from a short-range-ordered paramagnetic phase. Concomitantly, a small net magnetic moment evolves at T_N which points along the crystallographic c direction. Upon cooling, the net moment reorients at $T^{**} \simeq 1.7$ K and $T^* \simeq 1$ K. A broad 1/3 plateau indicative of the up-up-down (*uud*) spin configuration appears for magnetic fields $B\|c$ but is absent for $B\|ab$, thereby suggesting easy-axis anisotropy. At $T = 0.4$ K, a jump in magnetization at $\simeq 3/5$ of the saturation magnetization signals a discontinuous transition to a high field phase and we find evidence for a possible tricritical point. Small energy and field scales in the accessible regimes render $GdInO_3$ a well-suited example to study the phase diagram of a semiclassical frustrated hexagonal lattice in the presence of weak easy-axis anisotropy of mainly dipolar origin.

DOI: 10.1103/PhysRevB.108.224403

I. INTRODUCTION

Due to a wealth of relevant physical properties, perovskite rare-earth (RE) oxides with the nominal composition RBO_3 (R a RE ion) form a versatile class of materials and are a major topical research area in condensed-matter physics and materials science. Prominent examples of spectacular phenomena observed in this class of materials are metal-insulator transitions in rare-earth nickelates [1,2], colossal magnetoresistance, phase separation, or charge and orbital order in manganates [3–6] or multiferroicity in $RMnO_3$ [7,8]. Similar to hexagonal $RMnO_3$, the hexagonal $RInO_3$ (R = Eu, Gd, Tb, Dy, and Ho) systems crystallize in the $P6_3cm$ space group [9,10]. Their centered honeycomb lattice structure renders $RInO_3$ a well-suited platform to study geometrically frustrated magnets. Prior to 2017, studies on $RInO_3$ were limited to polycrystalline samples [11]. Accessibility of macroscopic single crystals such as $GdInO_3$ [12], $TbInO_3$ [13,14], and Mn-doped $TbInO_3$ [15] has boosted the field as, for example, ferroelectricity and spin-liquid-like behavior were found in $TbInO_3$ [13,14]. In comparison to the quantum spin liquid candidate $TbInO_3$, the properties of $GdInO_3$ resemble more those of a Heisenberg-like frustrated system with only small anisotropy [16]. In particular, in Ref. [16] the presence of a 1/3 magnetization plateau is reported which was inferred from an anomaly in the isothermal magnetization curves at 1.8 K. The presence of an $M_s/3$ plateau is a typical feature of the up-up-down (*uud*) phase in triangular antiferromagnets [17–20]. In addition, $GdInO_3$ features ferroelectricity as confirmed by observation of the $P(E)$ hysteresis loop as well as a Z_6 vortex topological domain structure [12].

Volatilization of In_2O_3 has long been a major challenge for the preparation of $GdInO_3$ single crystals. In this work, we have mitigated this issue by employing the high-pressure optical floating-zone method and show that high-quality $GdInO_3$ single crystals are successfully grown when using a high oxygen pressure of 30 bar. Using the single crystals we have constructed the magnetic phase diagrams in the temperature regime down to 400 mK and in magnetic fields up to 14 T. In the zero magnetic field, distinct anomalies in the magnetization and specific heat signal the evolution of long-range magnetic order at $T_N = 2.1$ K. Applying the magnetic fields parallel to the c axis yields a 1/3 magnetization plateau in the isothermal magnetization which is centered at about 3 T. This magnetization plateau behavior is absent when the field is applied along the ab plane. The system also exhibits a small net magnetic moment along the c axis, weak easy-axis anisotropy, reorientation processes both in the zero magnetic field and driven by the field, and a discontinuous transition into a high-field phase.

II. EXPERIMENTAL METHODS

Polycrystalline $GdInO_3$ was synthesized by a standard solid-state reaction following Refs. [12,16]. Stoichiometric amounts of Gd_2O_3 and In_2O_3 powders were well mixed and calcined at 1350 °C for 24 h (air flow, ambient pressure). The resulting material was ground and sintered for three times to ensure a complete reaction. Polycrystalline rods were prepared by hydrostatically pressing the powders under a pressure of 60 MPa and annealing them for 36 h at 1400 °C. $GdInO_3$ single crystal was grown by using the high-pressure optical floating-zone furnace (HKZ, SciDre) as described

*ning.yuan@kip.uni-heidelberg.de
†klingeler@kip.uni-heidelberg.de

TABLE I. Growth parameters and phase analysis from the Rietveld refinement of the room-temperature powder XRD data of $GdInO_3$ single crystals from the literature [12,16] and reported at hand (HKZ).

	Laser[a]	Two-mirror[b]	HKZ[c]
Atmosphere	O_2	O_2	O_2
Flow rate (l/min)	0.1	0.2	0.1
O_2 pressure (bar)	9.5	9	30
Growth rate (mm/h)	5–10	10	10
Lattice parameter a(Å)	6.3301(4)	6.3433(3)	6.3451(3)
Lattice parameter c(Å)	12.3340(17)	12.3320(1)	12.3408(9)

[a]Grown by the laser floating zone furnace (Crystal Systems Inc.), see Ref. [12].
[b]Grown by a two-mirror optical floating zone furnace (IRF01-001-05, Quantum Design), see Ref. [16].
[c]Grown by the high-pressure optical floating zone furnace (HKZ, SCIDRE), this work.

below. The phase purity and crystallinity were studied by powder x-ray diffraction (XRD) and the back-reflection Laue method. XRD was performed at room temperature by means of a Bruker D8 Advance ECO diffractometer using Cu-Kα radiation ($\lambda = 1.5418$ Å). Data have been collected in the 2Θ range of 10°–90° with a 0.02° step size. Structure refinement was carried out using the FULLPROF SUITE by means of the Rietveld method [21]. Studies of DC magnetization at 1.8–300 K have been performed in a SQUID magnetometer (MPMS3, Quantum Design Inc.) and by employing the vibrating sample magnetometer option of a Physical Properties Measurement System (PPMS, Quantum Design Inc.). For studies at temperatures between 0.4 and 5 K, the iQuantum ^{3}He option of MPMS3 was used. A relaxation method was used to perform specific heat measurements in the PPMS.

III. RESULTS

A. $GdInO_3$ single crystal growth

Heavy volatilization of In_2O_3 and low surface tension of the melts challenges growth of macroscopic $GdInO_3$ single crystals. To suppress volatilization, the crystals reported here were grown under an oxygen pressure of 30 bar using the high-pressure floating-zone furnace (HKZ, SciDre) [22,23]. High pressure was maintained at an O_2 flow rate of 0.1 l/min. A xenon arc lamp operating at 5 kW was employed and the growth was performed inside a sapphire chamber. A relatively fast growth rate of 10 mm/h was chosen in order to further mitigate In_2O_3 volatilization. At slower growth rates, we observed significant amounts of deposited In_2O_3 volatiles (see Fig. S1(a) of the Supplemental Material (SM) [24]) adhering to the inner protection glass tube, thereby affecting the focusing of light and preventing stable growth.

Using an *in situ* temperature measurement by means of a two-color pyrometer [25,26], the temperature of the melting zone during the growth was determined to about 1750 °C. The feed and seed rods were counter-rotated at 20 rpm to improve homogeneity of the melt; both feed and seed rods were pulled at 10 mm/h. The obtained boule is shown in Fig. S1(b) in the SM [24]. Table I lists the growth parameters used in this work and those in previous studies, as well as the refined lattice parameters and further characteristics of the respective crystals.

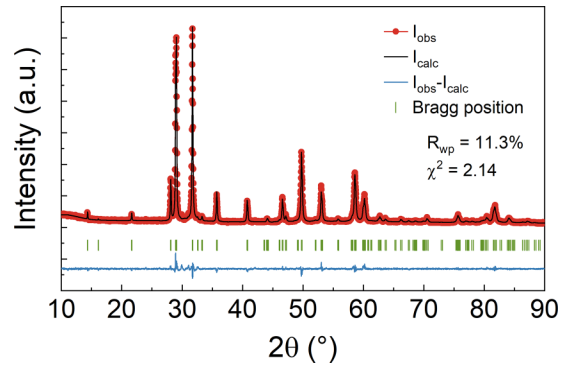

FIG. 1. Room-temperature XRD pattern and corresponding Rietveld refinement of powdered $GdInO_3$ single crystals grown at 30 bar O_2 pressure. The observed diffraction pattern is shown in red, the calculated one is shown in black, and the difference between them is shown in blue. Refinement is based on the hexagonal crystal system (space group $P6_3cm$, No. 185) of $GdInO_3$ as a main phase. The vertical green bars show the expected Bragg positions. The refinement converged to $R_p = 12.0\%$, $R_{wp} = 11.3\%$, and $\chi^2 = 2.14$.

A powder x-ray diffractogram on a ground single crystal as well as an Rietveld refinement to the data is shown in Fig. 1. The result of the XRD refinement demonstrates that our sample is free of impurities, and the lattice parameters and the crystal structure match the reported crystals [12,16]. Refined structural parameters are shown as Table S1 in the SM [24]. The x-ray Laue diffraction in back-scattering geometry was used to confirm single crystallinity and orient the single crystals, which were then cut with respect to the crystallographic main directions using a diamond-wire saw. Figure S1(c) [24] shows the single crystal sample used for the magnetic and specific heat measurements. The Laue pattern in Fig. S1(d) [24] illustrates the high crystallinity of this sample. Laue diffraction performed at several other pieces of the $GdInO_3$ boule which were cleaved at room temperature confirm that the dominant growth direction is in the *ab* plane.

The crystal structure of $GdInO_3$ is shown in Fig. 2. It belongs to the hexagonal space group $P6_3cm$ (No. 185), which alternately arranges corner-connected layered

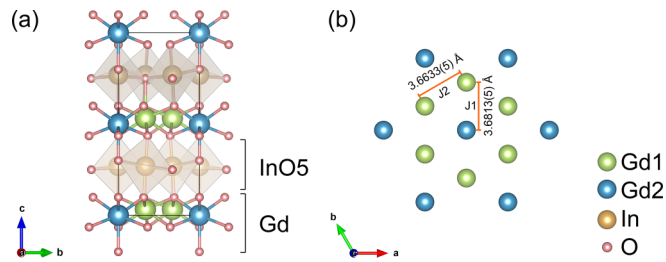

FIG. 2. (a) Schematic of the crystal structure of $GdInO_3$ along the [100] projection. (b) In-plane honeycomb arrangement of two inequivalent atomic sites of Gd^{3+} ions. J_1 and J_2 represent two magnetic exchange interactions that are distinguished by symmetry (COD No. 7237332 [12,27]).

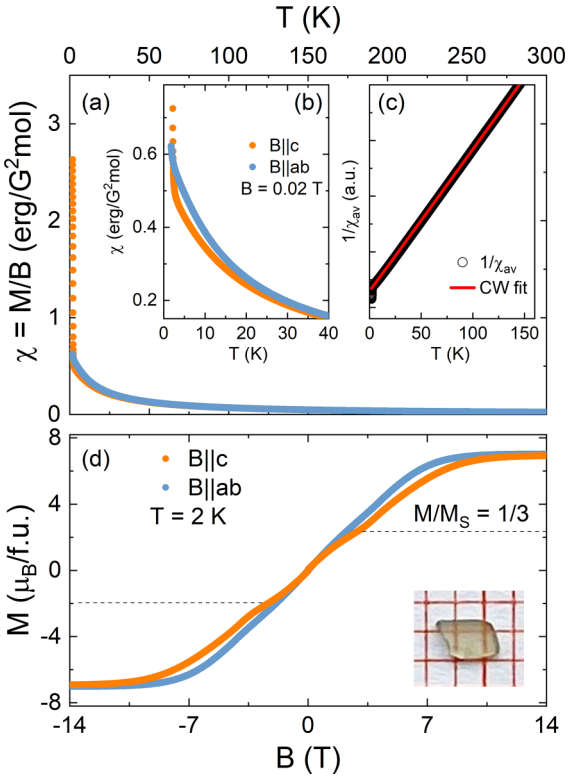

FIG. 3. (a) Temperature dependence of the static magnetic susceptibility $\chi = M/B$, obtained at $B = 0.02$ T applied along the crystallographic c axis ($B\|c$) and in-plane ($B\|ab$), respectively; panel (b) highlights small anisotropy at low temperatures. (c) Inverse of the averaged susceptibility $\chi_{\rm av} = (\chi_c + 2\chi_{ab})/3$ and Curie-Weiss fit (red line; see also Fig. S2 in the SM [24]). (d) Isothermal magnetization at $T = 2$ K for $B\|c$ and $B\|ab$. The horizontal dashed line marks 1/3 of the saturation magnetization. The inserted picture shows the oriented single crystal under study on a millimeter grid.

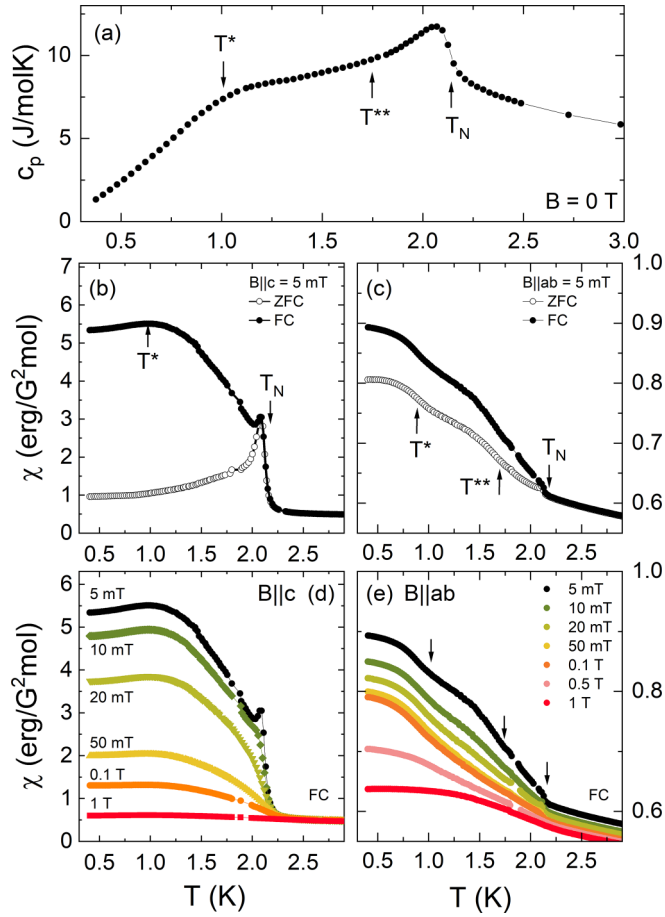

FIG. 4. (a) Specific heat at $B = 0$ T and static magnetic susceptibility $\chi = M/B$ in (b) $B\|c = 5$ mT and (c) $B\|ab = 5$ mT obtained in the field-cooled (FC) regime and the zero-field-cooled regime (ZFC) (black). (d, e) Static magnetic susceptibility (FC) at different external magnetic fields up to 1 T. $T_{\rm N}$, T^*, and T^{**} have been determined as described in the text.

InO_5 bipyramids and Gd layers. The structure features two inequivalent Gd sites in the Gd layers with Wyckoff positions 2a and 4b, respectively. The two types of Gd sites form an arc-like arrangement when viewed from the [100] direction [see Fig. 2(a)]. Hence, in the centered honeycomb layers formed by the Gd atoms in the plane perpendicular to the [001] axis, there are two slightly different Gd-Gd distances which may result in two distinct nearest-neighbor magnetic exchange parameters, J_1 (Gd1-Gd2) and J_2 (Gd1-Gd1) [see Fig. 2(b)] [11,16].

B. Magnetization $M(T, B)$

The static magnetic susceptibility $\chi = M/B$ obeys Curie-Weiss-like behavior down to about 50 K as shown in Figs. 3(a) and 3(c). At 300 K, $\chi(B\|ab)/\chi(B\|c) \simeq 1.01$ signals purely paramagnetic behavior and negligible anisotropy of the g factor. Upon cooling below ∼50 K, a small anisotropy between χ_c and χ_{ab} evolves before an anomaly at $T_{\rm N} = 2.1$ K indicates the onset of long-range magnetic order [see Fig. 3(b)]. Fitting the averaged susceptibility well above $T_{\rm N}$ by an extended Curie-Weiss law, i.e., $(\chi_c + 2\chi_{ab})/3 = \chi_0 + N_{\rm A} p_{\rm eff}^2/[3k_{\rm B}(T - \Theta)]$ with the Avogadro number $N_{\rm A}$ and the Boltzman constant $k_{\rm B}$ yields an excellent agreement with the data [Fig. 3(c)]. The fit yields the Weiss temperature $\Theta = -12(1)$ K and the effective magnetic moment $p_{\rm eff} = 7.9(1)\ \mu_{\rm B}$ which agrees with the theoretical value of 7.94 $\mu_{\rm B}$ for a free Gd^{3+} moment. The obtained negative Weiss temperature Θ implies predominant antiferromagnetic interactions. We note the frustration parameter $f = |\Theta|/T_{\rm N} \simeq 5$, which suggests considerable spin frustration in $GdInO_3$. Note that the experimental data deviate from the high-temperature Curie-Weiss fit below about 20 K as shown in Fig. S2 in the SM [24].

The onset of long-range antiferromagnetic (AF) order is associated with a clear anomaly in the specific heat shown in Fig. 4(a). Concomitantly and in agreement with the presence of a hysteresis in χ vs T, there is a steep increase of $\chi(B\|c)$ at $T_{\rm N}$ and pronounced hysteresis between the data obtained after cooling in the magnetic field (field-cooled; FC) and in the zero magnetic field (zero-field-cooled; ZFC) [see Figs. 4(b) and 4(c)]. Upon cooling, the FC static susceptibility ($\chi_{\rm FC}$) increases further until a broad maximum develops around $T^* \simeq 1$ K; below T^*, the magnetization $\chi(B\|c)$ slightly decreases. Concomitantly, there is a broad hump in the specific heat which has been interpreted as a signature of a second

antiferromagnetic phase appearing at T_{N2}, with $T_{N2} = 1.05$ K as indicated by the associated maximum in c_p/T [16]. This hump is clearly visible in our data in Fig. 4(a), too. We note, however, that the hump neither signals an entropy jump nor is it λ shaped, and hence, there is no clear signature of a thermodynamic phase transition at T^*. If one would alternatively interpret the hump as a broad jump in c_p, an entropy-conserving construction would suggest $T_{N2} \simeq 1.4$ K. At this temperature, however, there is no anomaly in the magnetization. As is discussed below, the observation of an anomaly in χ vs T and a maximum of a broad hump in c_p at the same temperature T^* may, hence, be considered a signature of crossover associated with reorientation of the spin structure. A reorientation process is not necessarily associated with a proper thermodynamic phase boundary (see, e.g., rotation of a small ferromagnetic moment in Eu_2CuSi_3 [28] and in $Gd_2In_{0.97}Si_{2.97}$ [29] where similar humps in c_p are observed).

The magnetization data imply hysteresis between FC and ZFC measurements at low temperatures with bifurcation below T_N. Both the increase of magnetization and hysteresis further confirm the presence of a weak ferromagnetic component below T_N. The tiny peak in χ_{FC} $(B\|c)$ is typical of a ferromagnetic-like domain state signaling decrease of magnetic anisotropy when heating towards the transition temperature. This scenario is supported by the observations in larger fields which suppress all features mentioned above, i.e., jump in magnetization, bifurcation, tiny peak, and the hump at T^*[see Fig. 4(b)].

Several features appear in $\chi(B\|ab)$ as demonstrated in Fig. 4(c): There is a kink at T_N indicating a very small increase of magnetization in the ordered phase. At T^*, there is a change in the slope as indicated by an inflection point in χ vs T. In addition, we observe an anomaly at $T^{**} \simeq 1.7$ K [see Fig. 4(c)]. Our data do not allow us to trace the field dependence $T^{**}(B\|ab)$. In contrast, T^* can be detected and it does not visibly change for small fields $B \leqslant 0.1$ T and increases for higher fields.

Further information on the long-range ordered phase is obtained by estimating the actual jump size of the specific heat anomaly at T_N. It is derived from the data by an entropy-conserving method to $\Delta c_p = 4.1(3)$ J/(mol K) [30]. This value is much smaller than the expected mean-field value for a $S = 7/2$ equal-moment system [31] of $\Delta c_p' = R\frac{5S(S+1)}{S^2+(S+1)^2} \simeq 20.1$ J/(mol K), with R being the gas constant [32]. Note that the actual jump size associated with the measured anomaly can be even smaller as it may be superimposed by critical fluctuations. The abovementioned mean-field result reduces to 2/3 of $\Delta c_p'$ in the case of amplitude-modulated spin configurations in which the amplitude of the magnetic moment varies periodically from one site to another [33]. Both predicted values are much larger than the experimentally observed anomaly, which implies significant short-range magnetic order above T_N (as, e.g., suggested by the frustration parameter $f \simeq 5$) and/or considerable spin disorder below T_N.

The magnetic entropy changes may be derived from the experimental specific heat data by subtracting the lattice contribution (c_p^{phonon}) which yields the magnetic specific heat c_{mag}. Fitting the data well above T_N by an Einstein-Debye model yields the characteristic temperatures $\Theta_D = 473$ K and $\Theta_E = 850$ K and describes the data well for temperatures above 30 K (see Fig. S7 in the SM [24]) [34]. Integrating $(c_p - c_p^{\text{ph}})/T$ yields the magnetic entropy changes of about 17.8(2) J/(mol K), which agrees with the theoretical expectation value of $R\ln 8 = 17.29$ J/(mol K). We note that only about 60% of the magnetic entropy is released at T_N while nearly 40% of the magnetic entropy is consumed between T_N and 20 K. This result implies significant short-range magnetic order persisting up to ten times the long-range ordering temperature. This is further confirmed by the fact that the experimentally observed magnetic susceptibility deviates from the high-temperature Curie-Weiss fit in the same temperature regime (see Fig. S2 in the SM [24]).

Notably, the mean-field description of entropy changes also implies the presence of a hump in c_p associated with low-energy excitations in the $J = 7/2$ multiplet, at $T/T_N \simeq 0.25$ [33,35]. Using $T_N = 2.1$ K predicts such a hump at ∼0.5 K, i.e., below T^* (see Fig. S6 in the SM [24]). Such a Schottky-like anomaly is typically observed in Gd-based systems with some variation of the temperature of its maximum [36–40]. Comparison of experimental data with the prediction of mean-field theory is shown as Fig. S8 in the SM [24]. Due to the fact that T_N does not meet the mean-field prediction either, one might attribute T^* to multiplet effects. However, our observation that $\chi(B\|c)$ decreases at T^* while $\chi(B\|ab)$ increases rather suggests the scenario of partial rotation of ferromagnetic component towards the ab plane. The fact that T^* is also characterized by a broad hump in the specific heat [Fig. 4(a)] then indicates that the changes in the magnetization in the ordered phase are associated with anomalous entropy changes.

The effect of magnetic fields on the magnetic ground state is further illustrated by the isothermal magnetization M vs B and the associated magnetic susceptibility $\partial M/\partial B$ at $T = 2$ K [up to 14 T: Fig. 3(d)]and at $T = 0.4$ K (up to 7 T: Fig. 5) as derived from the $M(B)$ curves. From $M(T = 2\,\text{K})$, similar values of the saturation magnetization M_s for the different field directions confirm rather isotropic g factors: 7.0(1) $(B\|ab)$ and 6.9(1) μ_B/f.u. $(B\|c)$. The saturation fields amount to $B_s^{ab} = 7.3(2)$ T and $B_s^c = 8.4(2)$ T. We also note several features in the $M(B)$ curves, the most prominent one appearing at around $M_s/3$ for $B\|c \simeq 2.9$ T.

At $T = 0.4$ K, the anomalies in the magnetization curves are most pronounced as displayed in Fig. 5 (full $M(B)$ curves covering -7 T $\leqslant B \leqslant 7$ T are shown as Fig. S3 in the SM [24]). The main features are as follows.

(i) There is a small ferromagnetic moment and magnetic hysteresis visible in the inset of Fig. 5(a) which show, for $B\|c$, a small remanent moment of 0.14 μ_B/f.u. and the critical field ≃60 mT. No indication of hysteresis is found for $B\|ab$, which, however, displays s-shaped behavior around $B = 0$ T as shown in the inset in Fig. 5(b) and by the broad peak in $\partial M/\partial B_{\|ab}$ centered at $B = 0$ T.

(ii) For $B\|c$, there is a plateau-like feature in M centered at $B_{c1} = 2.9$ T and a small jump in M at $B_{c2} = 5.5$ T. Above B_{c2}, $M(B)$ features linear behavior which extrapolates to its saturation value at $B_s \simeq 8.6$ T [41]. We also note a feature at $B_{c1}^{\nabla} = 4.2$ T signaling the onset of the linear-in-M regime and

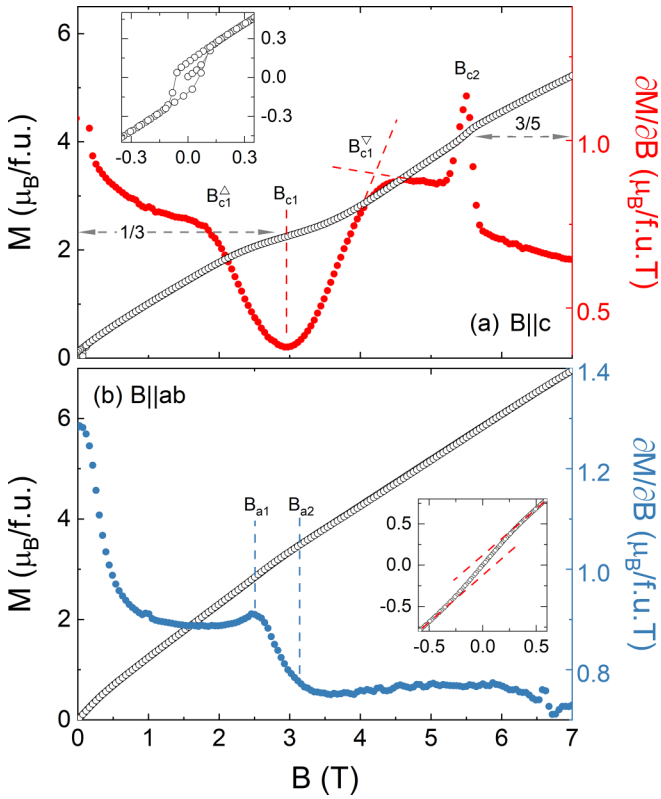

FIG. 5. Isothermal magnetization at $T = 0.4$ K for (a) the $B\|c$ axis and (b) the $B\|ab$ plane (left ordinates) and corresponding magnetic susceptibilities $\partial M/\partial B$ are shown (right ordinates). The full magnetization loop (from -7 to $+7$ T) is shown in Fig. S3 of the Supplemental Material [24]). Insets highlight the behavior around zero field. Horizontal dashed lines mark $M_s/3$ and $3M_s/5$; vertical lines show the anomaly fields as described in the text.

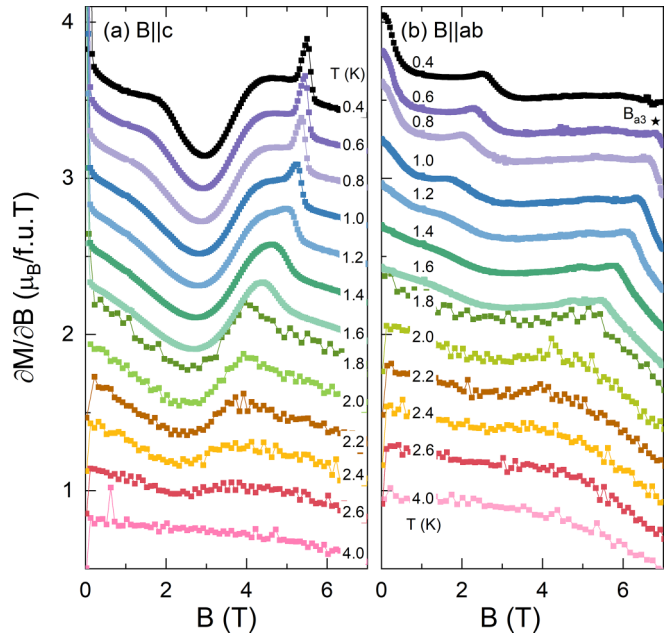

FIG. 6. Magnetic susceptibility $\partial M/\partial B$ for (a) $B\|c$ and (b) $B\|ab$ at different temperatures. The curves are offset vertically by 0.23 μ_B/(f.u. T) for better visibility; the dashed line in panel (b) indicates the evolution of B_{a3}.

thus the upper limit of the plateau region while the plateau's lower edge is marked $B_{c1}^{\triangle}$.

(iii) For $B\|ab$, there is a jump in $\partial M/\partial B$ at $B_{a1} \simeq 2.5$ T which is preceded by a tiny peak (i.e., a small jump in M) at B_{a1} and followed by a linear regime in M for $B > B_{a2}$.

To summarize the main features, there is a clear magnetization plateau visible in $M(B\|c)$, extending from $B_{c1}^{\triangle}$ to B_{c1}^{∇} and centered at B_{c1}, which perfectly agrees with 1/3 of the saturation magnetization as determined at 2 K [cf. Fig. 3(d)]. Note that we find M_s rather independent of temperature in the accessible temperature regime so that M_s (2 K) $\simeq$ M_s (0.4 K). A similar conclusion on the presence of a 1/3 magnetization plateau has been drawn from magnetization data at 1.8 K in Ref. [16]. In addition, there is a small jump in M at B_{c2} signaling a discontinuous phase transition at about $3/5M_s$. We also note that the tiny peak in $\partial M/\partial B_{\|ab}$ at B_{a1} appears at 2/5 of the saturation magnetization, and B_{a2} which signals the onset of a linear regime in $M(B > B_{a2})$ appears at $\simeq$1/2 of M_s.

C. Magnetic phase diagrams

Distinct anomalies in M vs B allow us to trace the temperature dependence of the phase boundaries associated with the critical fields marked in Fig. 5. Specifically, we have used the anomalies of the magnetic susceptibility shown in Fig. 6 to construct the magnetic phase diagrams. In addition, we have derived the saturation fields from our $M(B, T \geqslant 1.8\,\text{K})$ data up to 14 T (see Fig. 3(d) and Figs. S3 and S5 in the SM [24]) and from extrapolating the linear-in-field behavior at 0.4 K $\leqslant T \leqslant$ 1.8 K, as well as T_N (B), $T^*(B)$, and $T^{**}(B)$ at low fields from M vs T measurements (see Fig. 4). The resulting phase diagrams are shown in Fig. 7. The following main features appear for $B\|c$. Centered at B_{c1}, a 1/3 magnetization plateau is formed which starts to evolve at $B_{c1}^{\triangle}$ and extends to B_{c1}^{∇}. B_{c1} is barely temperature dependent as it only slightly shifts to lower fields upon heating. Below about 1.2 K, there is a linear-in-B regime of the magnetization following the AF I/plateau phase. Whether the AF I/AF I′/AF I″ boundaries signal proper thermodynamic phase transitions or crossover regimes is yet unclear. A sharp jump in M at B_{c2} clearly indicates a discontinuous phase transition and suggests a flip of the spin configuration. This jump is superimposed by a kink in M vs T as demonstrated by the peak and superimposed jump in $\partial M/\partial B$ in Fig. 5. Upon heating, the sharp peak in $\partial M/\partial B$ evolves to a broader feature in the temperature region where the upper boundary of the plateau phase (B_{c1}^{∇}) merges with B_{c2}. Broadening and softening of the anomaly may indicate that the phase boundary evolves towards a continuous nature, which would suggest the presence of a tricritical point at $\simeq$4 T and $\simeq$1.6 K.

The Clausius-Clapeyron equation enables us to estimate the entropy changes appearing at the AF I′/AF II phase boundary [42]:

$$\Delta S_{c2} = -\Delta M_{c2} \frac{\partial B_{c2}}{\partial T}. \quad (1)$$

Using $\Delta M(0.4\,\text{K}) \simeq 0.11(1)$ μ_B/f.u., the analysis yields $\Delta S_{c2} \simeq 0.15(3)$ J/(mol K), at 0.4 K.

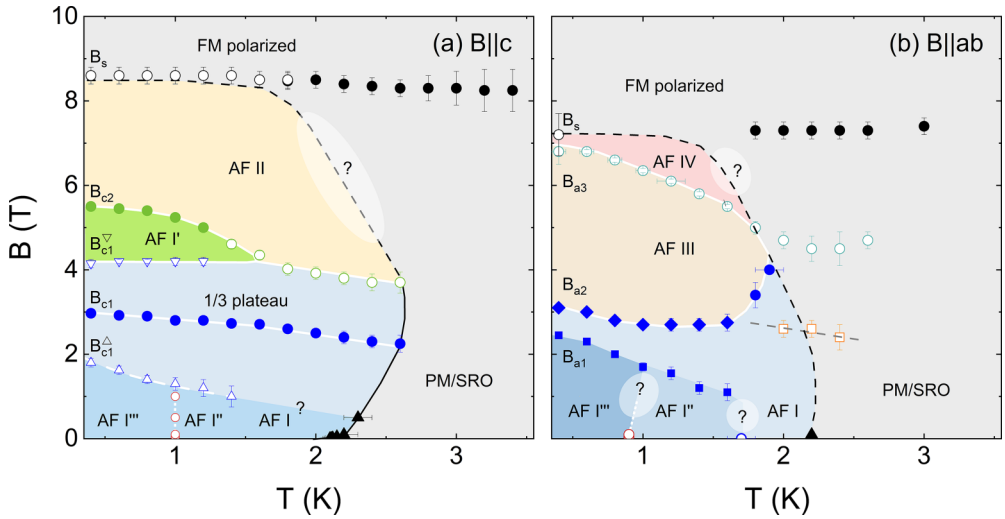

FIG. 7. Magnetic phase diagram of $GdInO_3$ for $B\|c$ and $B\|ab$. $B_{a/ci}$ mark the critical fields as defined in Fig. 5 and in the text. $B\|c$: AF I: Low-field AF phase; 1/3 plateau phase centered around B_{c1} and confined by $B_{c1}^{\triangle}$ and $B_{c1}^{\triangledown}$. The latter marks the onset of a linear-in-M regime AF I′. At B_{c2} a small jump in M appears before the polarized regime is achieved at B_s. $B\|ab$: At $B = 0$ T, several features distinguish regions of different spin-orientation (AF I, AF I″, AF I‴). A clear phase boundary B_{a1} (T) separates AF I‴ from the higher-field phase which may extend to AF I. Two AF phases (AF I and AF III) are separated by B_{a2}. A further kink in M marks the onset of a high-field but not fully polarized phase AF IV at B_{a3}. Several features appearing in the paramagnetic/short-range ordered phase (PM/SRO) are shown, too, as well as the regimes AF I, AF I″, and AF I‴. White areas mark regions where the phase boundaries are yet unclear.

As described above, for $T > 1.2$ K, the sharp peak transforms into a much broader feature and B_{c2} is suppressed upon further heating. The saturation field towards the ferromagnetically polarized phase does not display strong temperature dependence and the saturation features can be traced well above the long-range ordered phase. We attribute this to significant short-range magnetic correlations above T_N. In contrast to B_s, magnetization measurements do not detect the phase boundary T_N $(B > 4$ T), indicating that the magnetization in AF II and in the short-range ordered phase is very similar in this field regime. One may speculate about the phase boundary as suggested in Fig. 7(a).

We note that the magnetization M_c increases at T_N ($\simeq$0 T), which already implies the observed positive initial field dependence of the associated phase boundary. Quantitatively, it may be estimated using the Ehrenfest equation:

$$\frac{\partial T_N}{\partial B} = -T_N \frac{\Delta M'}{\Delta c_p}. \tag{2}$$

Exploiting the experimentally determined jump in specific heat Δc_p from Fig. 4(a) and the change in slope of magnetization $\Delta M' = \Delta(\partial M/\partial T)$ yields $\partial T_N/\partial B_{\|c} = 1.7(2)$ K/T, which is consistent with our data T_N $(B \gtrsim 0$ T) shown in Fig. 7(a).

For $B\|ab$ [Fig. 7(b)], we observe no sizable field dependence of T_N in small magnetic fields. This agrees with the observation of only a small increase of M_{ab} at T_N. The quantitative analysis in terms of the Ehrenfest relation [Eq. (2)] yields only $\partial T_N/\partial B \simeq 0.02(1)$ K/T. At zero field, two further anomalies in $M(T)$ [Fig. 4(c)] indicate rotation of the ferromagnetic component. The related regimes in the phase diagram are labeled AF I″ and AF I‴ and the nature of the boundaries is not clear [Fig 7(b)].

A small peak and a subsequent jump in $\partial M/\partial B_{\|ab}$ [see Fig. 5(b)] signal the appearance of the high-field phase AF III. From the fact that both anomalies B_{a1} and B_{a2} further separate upon heating, we conclude that the intermediate phase extends to the AF I regime at $B = 0$ T. While AF I is separated by distinct anomalies from AF III around 2 K, B_{a1} cannot be traced up to T_N. T_N (B) cannot be well traced by our data either. In contrast, the upper phase boundary of AF III, i.e., B_{a3}, is marked by clear anomalies in $\partial M(B)\partial B$ as indicated in Fig. 6, where associated kinks are visible for $T \geqslant 0.6$ K. From the fact that B_s seems to be rather independent of temperature and clearly exceeds or is distinct from B_{a3}, we conclude the presence of the high-field phase AF IV [43]. The nature of AF IV is yet unknown. Note that again several features in $M(B)$ extend into the short-range ordered/paramagnetic phase.

Finally, we discuss the phase diagram in the frame of potential spin configurations appearing in triangular-lattice spin systems (see, e.g., Refs. [19,20,44,45]). The ground-state spin configuration has not yet been determined experimentally. Potential candidates of the ground-state configuration are coplanar Y-type (as also discussed in Ref. [16]) or umbrella-type configurations. In both cases, finite-temperature *uud* phases may appear [45,46].

(i) Our experimental data imply the presence of a net magnetic moment. In the case of the Y-type configuration, the measured net moment would correspond to an angle of $2\theta \simeq 117^\circ$ between the upper spins in Fig. 8(a). An umbrella structure would feature a huge aperture outside the *ab* plane [see Fig. 8(b)]; the observed size of the canted moment would suggest an angle of $\simeq 1.2^\circ$ between the Gd moments and the *ab* plane [47]. The in-plane projections of the moments cancel out in this scenario. The data in Fig. 4 indicate partial rotation of the net moment towards the *ab* plane, yielding further

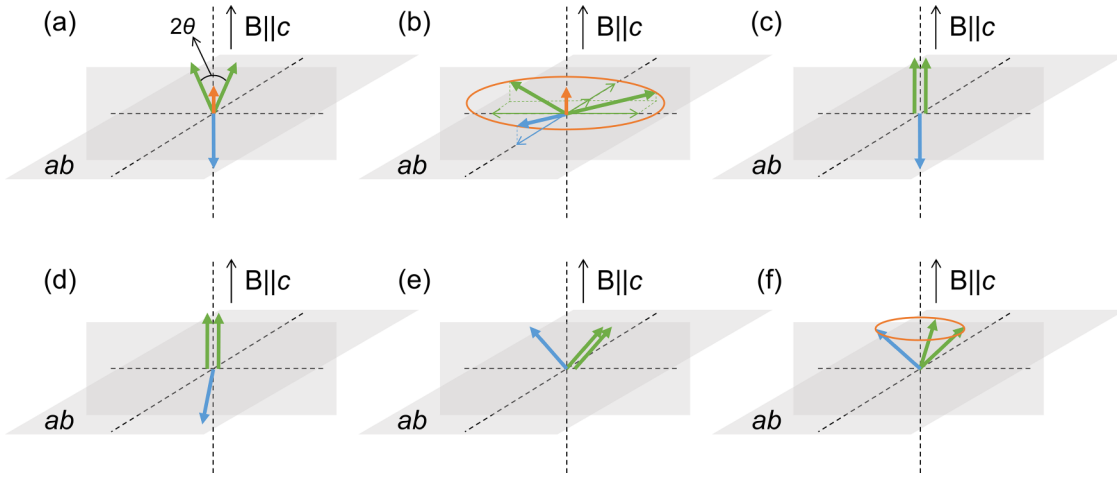

FIG. 8. Schematic diagram of possible spin configurations in $GdInO_3$ in different magnetic fields. The green and blue arrows indicate the spin directions at the Gd1 and Gd2 positions, respectively, which correspond to the Gd atom positions in Fig. 2. The orange arrows indicate the net magnetic moment along the c axis. The angle between the upward spins in panel (a) is denoted by 2θ.

distortions of the abovementioned configurations. From Fig. 4(c) we conclude that this rotation appears in two steps at $\simeq$1.7 K and $\simeq$1 K, respectively. Small external magnetic field $B\|c$ yields a ferromagnetic-like hysteresis [see Fig. 5(a)] with the c axis being the magnetic easy axis of the net moment.

(ii) Applying intermediate fields $B\|c$ yields the formation of a colinear *uud* configuration [Fig. 8(c)], i.e., the plateau phase. At 0.4 K, the plateau region is centered at 2.9 T and extends from 1.9–4.2 T [Fig. 5(a)]. Our finding of a smeared-out and not completely flat plateau only for $B\|c$ does support the scenario of a classical Heisenberg triangular-lattice antiferromagnet (TLAF) with easy-axis anisotropy [48] as discussed, e.g., for $Na_2BaCo(PO_4)_2$ [49], $Rb_4Mn(MoO_4)_3$ [50], $GdPd_2Al_3$ [51], $Ba_3MnNb_2O_9$ [18], and $Ba_3NiSb_2O_9$ [52]. The center and edges of the plateau phase do not strongly change upon heating. However, the plateau significantly blurs and no clear signature of $B_{c1}^{\triangle}$ can be identified above $\simeq$1.5 K.

(iii) Above $B_{c1}^{\triangledown}$, the linear increase in M implies breaking of the *uud* configuration and the continuous alignment of spins towards the field [Fig. 8(d)]. A similar behavior is predicted in Ref. [48]; in agreement with these numerical studies, phase AF I′ is found to be destabilized in external fields $B\|c$.

(iv) In contrast to the predictions of the minimal TAF model [48], we observe an additional discontinuity at B_{c2} associated with a jump-like increase of magnetization. The jump is from about 4.1 to nearly 4.2 μ_B/f.u., i.e., it starts at about 3/5 of the full saturation magnetization. In this magnetization regime, there are several possible scenarios which may account for such behavior. One of which includes discontinuous rotation of the *uu* moments from the easy direction towards a coplanar V-shaped structure which may evolve from the *uud* phase by decreasing the angle $\angle(uu, d)$ as sketched in Fig. 8(e). However, our data do not allow to unambiguously resolve the spin configurations in this field range.

(v) For $B\|ab$, no plateau phase is formed. Instead, we observe a small kink and a jump in $\partial M/\partial B$, at B_{a1} and B_{a2} [see Fig. 5(b)]. Note that the magnetization at B_{a1} and B_{a2} amounts to 2.79(5) μ_B/f.u. and 3.45(5) μ_B/f.u., respectively, which is very similar to 2/5 and 1/2 of the saturation values. Due to the presence of several rotated spin arrangements (rotations at $\simeq$1.7 K and $\simeq$1 K), only rough speculations on the field effects are possible. The behavior of $M(B\|ab)$ around $B = 0$ T, however, shows that the net magnetic moment is rather smoothly aligned into the *ab* plane. The origin of the further distinct phases in the magnetic phase diagram Fig. 7(b) remains to be clarified.

In TLAFs with classical spins, both easy-axis anisotropy and easy-plane anisotropy can stabilize the *uud* phase at finite temperatures (see, e.g., Refs. [18,53]). The presence of the 1/3 plateau in $GdInO_3$ implies that such easy-axis and easy-plane anisotropy, which lift geometric frustration, are relevant for driving the system into the *uud* configuration. Comparing the temperature evolution of the *uud* phase for $B\|c$ with numerical studies [48] suggests that $GdInO_3$ has a weak easy-axis anisotropy. This conclusion is corroborated by the absence of the 1/3 magnetization plateau for $B\|ab$. It is also in-line with model calculations of the magnetization of $GdInO_3$ in Ref. [16] where weak easy-axis anisotropy $D > 0$ and $J_1 \geqslant J_2$ are suggested.

Anisotropy can arise from dipolar interactions between the Gd^{3+} moments within the filled honeycomb layer. Dipole-dipole interaction can be described by the following Hamiltonian [54]:

$$\mathcal{H}_{\rm dip} = g^2\mu_B^2 \sum_{i<j} \left[\mathbf{S_i}\mathbf{S_j}/r_{ij}^3 - 3(\mathbf{S_i}\mathbf{r_{ij}})(\mathbf{S_j}\mathbf{r_{ji}})/r_{ij}^5\right], \quad (3)$$

with $\mathbf{r_{ij}}$ being the vector between interacting paramagnetic centers and r_{ij} the distance between them, such that the dipolar anisotropy $D_{\rm dip}$ can be estimated as $D_{\rm dip} = E_{\rm dip}/S^2 = \mu_B^2 p_{\rm eff}^2 \mu_0/4\pi r^3 S^2$. The resulting dipole-dipole energy amounts to $E_{\rm dip} = \mu_B^2 p_{\rm eff}^2 \mu_0/4\pi r^3 = 0.78(2)$ K, with the weighted average $r_{\rm ave} = (2r_1 + r_2)/3 = 3.6753(5)$ calculated from the distances $r_1 = 3.6813(5)$ and $r_2 = 3.6633(5)$ from our structure refinement. This energy roughly corresponds to T^* and T^{**} where reorientation processes are observed. Similar anisotropy energies for Gd^{3+} systems were reported

in the literature for $(Y_{1-x}Gd_x)_2Ti_2O_7$ [55] and $Gd_2Ti_2O_7$ [56]. However, exchange interaction may be also relevant in this system, and its relevance in $GdInO_3$ and in particular for the presence of the presumingly anisotropy-related 3/5 discontinuity should be investigated by numerical studies.

IV. SUMMARY

By means of single crystals grown by the high-pressure optical floating-zone method, the magnetization process down to the mK regime and the magnetic phase diagrams of $GdInO_3$ have been investigated. The system evolves long-range antiferromagnetic order at $T_N = 2.1$ K and exhibits considerable magnetic frustration ($|\Theta|/T_N \simeq 5$). The ground state features a small net magnetic moment along the crystallographic c direction which reorients upon cooling at $T^{**} \simeq 1.7$ K and $T^* \simeq 1$ K. A broad 1/3 plateau indicative of the *uud* spin configuration appears for $B\|c$ but is absent for $B\|ab$, thereby suggesting easy-axis anisotropy. In this respect $GdInO_3$ is a typical triangular-lattice material in which weak easy-axis anisotropy of presumingly dipolar nature breaks C_3 symmetry and allows formation of the *uud* phase. In addition, a jump in magnetization at low temperatures signals a discontinuous transition to a high-field phase. There is evidence that the transition evolves a continuous nature upon heating via a possible tricritical point. Small energy and field scales in the accessible regimes render $GdInO_3$ a well-suited example to study the phase diagram of a semiclassical frustrated hexagonal lattice in the presence of weak easy-axis anisotropy, e.g., by future neutron diffraction studies, to verify the actual spin configurations in the various thermodynamic phases.

ACKNOWLEDGMENTS

Support by Deutsche Forschungsgemeinschaft (DFG) under Germany's Excellence Strategy EXC2181/1-390900948 (The Heidelberg STRUCTURES Excellence Cluster) and through Project No. KL 1824/13-1 is gratefully acknowledged. N.Y. acknowledges support from a fellowship by the Chinese Scholarship Council (File No. 201906890005).

[1] A. Mercy, J. Bieder, J. Íñiguez, and P. Ghosez, Nat. Commun. **8**, 1677 (2017).
[2] R. D. Sánchez, M. T. Causa, A. Caneiro, A. Butera, M. Vallet-Regi, M. J. Sayagués, J. González-Calbet, F. Garcia-Sanz, and J. Rivas, Phys. Rev. B **54**, 16574 (1996).
[3] A. Ramirez, J. Phys.: Condens. Matter **9**, 8171 (1997).
[4] M. Uehara, S. Mori, C. Chen, and S.-W. Cheong, Nature (London) **399**, 560 (1999).
[5] C. N. R. Rao, A. Arulraj, P. N. Santosh, and A. K. Cheetham, Chem. Mater. **10**, 2714 (1998).
[6] S. Uhlenbruck, R. Teipen, R. Klingeler, B. Büchner, O. Friedt, M. Hücker, H. Kierspel, T. Niemöller, L. Pinsard, A. Revcolevschi *et al.*, Phys. Rev. Lett. **82**, 185 (1999).
[7] T. Choi, Y. Horibe, H. Yi, Y. J. Choi, W. Wu, and S.-W. Cheong, Nat. Mater. **9**, 253 (2010).
[8] B. B. Van Aken, T. T. Palstra, A. Filippetti, and N. A. Spaldin, Nat. Mater. **3**, 164 (2004).
[9] E. E. Gordon, X. Cheng, J. Kim, S.-W. Cheong, S. Deng, and M.-H. Whangbo, Inorg. Chem. **57**, 9260 (2018).
[10] Y. Yu, N. Lin, H. Wang, R. Xu, H. Ren, and X. Zhao, RSC Adv. **10**, 4080 (2020).
[11] B. Paul, S. Chatterjee, A. Roy, A. Midya, P. Mandal, V. Grover, and A. K. Tyagi, Phys. Rev. B **95**, 054103 (2017).
[12] Y. Li, Y. Wang, W. Tan, W. Wang, J. Zhang, J. W. Kim, S.-W. Cheong, and X. Tao, J. Mater. Chem. C **6**, 7024 (2018).
[13] L. Clark, G. Sala, D. D. Maharaj, M. B. Stone, K. S. Knight, M. T. Telling, X. Wang, X. Xu, J. Kim, Y. Li *et al.*, Nat. Phys. **15**, 262 (2019).
[14] J. Kim, X. Wang, F.-T. Huang, Y. Wang, X. Fang, X. Luo, Y. Li, M. Wu, S. Mori, D. Kwok *et al.*, Phys. Rev. X **9**, 031005 (2019).
[15] M. G. Kim, B. Winn, S. Chi, A. T. Savici, J. A. Rodriguez-Rivera, W. C. Chen, X. Xu, Y. Li, J. W. Kim, S. W. Cheong, and V. Kiryukhin, Phys. Rev. B **100**, 024405 (2019).
[16] X. Yin, Y. Li, G. Wang, J. Hu, C. Xu, Q. Lu, Y. Zhong, J. Zhao, X. Zhao, Y. Zhang *et al.*, Phys. Rev. B **104**, 134432 (2021).
[17] L. Seabra, T. Momoi, P. Sindzingre, and N. Shannon, Phys. Rev. B **84**, 214418 (2011).
[18] M. Lee, E. S. Choi, X. Huang, J. Ma, C. R. Dela Cruz, M. Matsuda, W. Tian, Z. L. Dun, S. Dong, and H. D. Zhou, Phys. Rev. B **90**, 224402 (2014).
[19] T. Susuki, N. Kurita, T. Tanaka, H. Nojiri, A. Matsuo, K. Kindo, and H. Tanaka, Phys. Rev. Lett. **110**, 267201 (2013).
[20] L. E. Svistov, A. I. Smirnov, L. A. Prozorova, O. A. Petrenko, A. Micheler, N. Büttgen, A. Y. Shapiro, and L. N. Demianets, Phys. Rev. B **74**, 024412 (2006).
[21] J. Rodríguez-Carvajal, *An Introduction to the Program* FULLPROF 2000 (Laboratoire Leon Brillouin, CEA-CNRS, Saclay, France, 2001).
[22] N. Wizent, G. Behr, F. Lipps, I. Hellmann, R. Klingeler, V. Kataev, W. Löser, N. Sato, and B. Büchner, J. Cryst. Growth **311**, 1273 (2009).
[23] C. Neef, H. Wadepohl, H.-P. Meyer, and R. Klingeler, J. Cryst. Growth **462**, 50 (2017).
[24] See Supplemental Material at http://link.aps.org/supplemental/10.1103/PhysRevB.108.224403 for further information on the grown crystal and additional magnetization data.
[25] W. Hergett, C. Neef, H. Wadepohl, H.-P. Meyer, M. M. Abdel-Hafiez, C. Ritter, E. Thauer, and R. Klingeler, J. Cryst. Growth **515**, 37 (2019).
[26] W. Hergett, C. Neef, H.-P. Meyer, and R. Klingeler, J. Cryst. Growth **556**, 125995 (2021).
[27] K. Momma and F. Izumi, J. Appl. Crystallogr. **44**, 1272 (2011).
[28] C. D. Cao, R. Klingeler, H. Vinzelberg, N. Leps, W. Löser, G. Behr, F. Muranyi, V. Kataev, and B. Büchner, Phys. Rev. B **82**, 134446 (2010).
[29] S. Chakraborty, S. Gupta, S. Pakhira, R. Choudhary, A. Biswas, Y. Mudryk, V. K. Pecharsky, D. D. Johnson, and C. Mazumdar, Phys. Rev. B **106**, 224427 (2022).
[30] R. Ohlendorf, S. Spachmann, L. Fischer, K. Dey, D. Brunt, G. Balakrishnan, O. A. Petrenko, and R. Klingeler, Phys. Rev. B **103**, 104424 (2021).

[31] Equal-moment systems are magnetic structures of equal-size moments such as Neel-type, helical, or cycloidal antiferromagnets.
[32] A. H. Morrish, *The Physical Principles of Magnetism* (IEEE, Piscataway, NJ, 2001).
[33] J. A. Blanco, D. Gignoux, and D. Schmitt, Phys. Rev. B **43**, 13145 (1991).
[34] In Ref. [16] a more extended background fit with additional fitting parameters has been applied which yields similar yet slightly smaller entropy changes.
[35] D. C. Johnston, Phys. Rev. B **91**, 064427 (2015).
[36] D. C. Johnston, J. Magn. Magn. Mater. **535**, 168062 (2021).
[37] S. Manni, S. L. Bud'ko, and P. C. Canfield, Phys. Rev. B **96**, 054435 (2017).
[38] T. Kong, W. R. Meier, Q. Lin, S. M. Saunders, S. L. Bud'ko, R. Flint, and P. C. Canfield, Phys. Rev. B **94**, 144434 (2016).
[39] E. Mun, S. Bud'ko, H. Ko, G. Miller, and P. Canfield, J. Magn. Magn. Mater. **322**, 3527 (2010).
[40] H. Hidaka, K. Mizuuchi, E. Hayasaka, T. Yanagisawa, J. Ohara, and H. Amitsuka, Phys. Rev. B **102**, 174408 (2020).
[41] Note that applying the same method at 1.8 K where the saturation field has been determined experimentally (see Fig. 3), i.e., extrapolating the linear regime at 1.8 K, yields a value of B_s which agrees well with the saturation field derived from the actual measurements up to 14 T at this temperature.
[42] T. H. K. Barron and G. K. White, *Heat Capacity and Thermal Expansion at Low Temperatures*, The International Cryogenic Monograph Series (Kluwer Academic/Plenum, New York, 1999).
[43] Extrapolating the experimental data $M(B \leqslant 7\mathrm{T})$ to higher fields as done for $B\|c$ in order to estimate B_s only yields ambiguous results due to pronounced bending of $M(B)$ in this regime. We, hence, do not apply this method for $B\|ab$.
[44] T. Ono, H. Tanaka, H. Aruga Katori, F. Ishikawa, H. Mitamura, and T. Goto, Phys. Rev. B **67**, 104431 (2003).
[45] O. A. Starykh, Rep. Prog. Phys. **78**, 052502 (2015).
[46] C. Griset, S. Head, J. Alicea, and O. A. Starykh, Phys. Rev. B **84**, 245108 (2011).
[47] For a sketch illustrating the calculation of the relevant angles, see Fig. S9 in the SM [24].
[48] S. Miyashita, J. Phys. Soc. Jpn. **55**, 3605 (1986).
[49] N. Li, Q. Huang, X. Yue, W. Chu, Q. Chen, E. Choi, X. Zhao, H. Zhou, and X. Sun, Nat. Commun. **11**, 4216 (2020).
[50] R. Ishii, S. Tanaka, K. Onuma, Y. Nambu, M. Tokunaga, T. Sakakibara, N. Kawashima, Y. Maeno, C. Broholm, D. P. Gautreaux *et al.*, Europhys. Lett. **94**, 17001 (2011).
[51] H. Kitazawa, H. Suzuki, H. Abe, J. Tang, and G. Kido, Phys. B: Condens. Matter **259-261**, 890 (1999).
[52] Y. Shirata, H. Tanaka, T. Ono, A. Matsuo, K. Kindo, and H. Nakano, J. Phys. Soc. Jpn. **80**, 093702 (2011).
[53] M. Lee, J. Hwang, E. S. Choi, J. Ma, C. R. Dela Cruz, M. Zhu, X. Ke, Z. L. Dun, and H. D. Zhou, Phys. Rev. B **89**, 104420 (2014).
[54] A. Bencini and D. Gatteschi, *EPR of Exchange Coupled Systems* (Dover, Mineola, NY, 2012).
[55] V. N. Glazkov, M. E. Zhitomirsky, A. I. Smirnov, H.-A. Krug von Nidda, A. Loidl, C. Marin, and J.-P. Sanchez, Phys. Rev. B **72**, 020409(R) (2005).
[56] N. P. Raju, M. Dion, M. J. P. Gingras, T. E. Mason, and J. E. Greedan, Phys. Rev. B **59**, 14489 (1999).